Non-contrast free-breathing whole-heart 3D cine cardiovascular magnetic resonance with a novel 3D radial leaf trajectory

Braunstorfer, L.; Romanowicz, J.; Powell, A.J.; Pattee, J.; Browne, L.P.; Geest, R.J. van der; Moghari, M.H.

Magnetic Resonance Imaging 94 (2022) 64–72

Contents lists available at ScienceDirect

Magnetic Resonance Imaging

journal homepage: www.elsevier.com/locate/mri

Non-contrast free-breathing whole-heart 3D cine cardiovascular magnetic resonance with a novel 3D radial leaf trajectory

Lukas Braunstorfer [a,b,*], Jennifer Romanowicz [a,d], Andrew J. Powell [a], Jack Pattee [e], Lorna P. Browne [f], Rob J. van der Geest [c], Mehdi H. Moghari [f]

[a] Department of Cardiology, Boston Children's Hospital, Department of Pediatrics, Harvard Medical School, Boston, MA, USA
[b] Department of Informatics, Technical University of Munich, Munich, BY, Germany
[c] Department of Radiology, Leiden University Medical Center, Leiden, the Netherlands
[d] Department of Pediatrics, Section of Cardiology, Children's Hospital Colorado, School of Medicine, The University of Colorado, CO, USA
[e] Department of Biostatistics and Informatics, Colorado School of Public Health, CO, USA
[f] Department of Radiology, Children's Hospital Colorado, and School of Medicine, The University of Colorado, CO, USA

ARTICLE INFO

Keywords:
Non-contrast
Free-breathing
Whole-heart
3D cine
Cardiovascular magnetic resonance
Ventricular function
And 3D radial trajectory

ABSTRACT

Purpose: To develop and validate a non-contrast free-breathing whole-heart 3D cine steady-state free precession (SSFP) sequence with a novel 3D radial leaf trajectory.
Methods: We used a respiratory navigator to trigger acquisition of 3D cine data at end-expiration to minimize respiratory motion in our 3D cine SSFP sequence. We developed a novel 3D radial leaf trajectory to reduce gradient jumps and associated eddy-current artifacts. We then reconstructed the 3D cine images with a resolution of 2.0mm^3 using an iterative nonlinear optimization algorithm. Prospective validation was performed by comparing ventricular volumetric measurements from a conventional breath-hold 2D cine ventricular short-axis stack against the non-contrast free-breathing whole-heart 3D cine dataset in each patient ($n = 13$).
Results: All 3D cine SSFP acquisitions were successful and mean scan time was 07:09 ± 01:31 min. End-diastolic ventricular volumes for left ventricle (LV) and right ventricle (RV) measured from the 3D datasets were smaller than those from 2D (LV: 159.99 ± 42.99 vs. 173.16 ± 47.42; RV: 180.35 ± 46.08 vs. 193.13 ± 49.38; p-value$\leq$0.044; bias<8%), whereas ventricular end-systolic volumes were more comparable (LV: 79.12 ± 26.78 vs. 78.46 ± 25.35; RV: 97.18 ± 32.35 vs. 102.42 ± 32.53; p-value$\geq$0.190, bias<6%). The 3D cine data had a lower subjective image quality score.
Conclusion: Our non-contrast free-breathing whole-heart 3D cine sequence with novel leaf trajectory was robust and yielded smaller ventricular end-diastolic volumes compared to 2D cine imaging. It has the potential to make examinations easier and more comfortable for patients.

1. Introduction

The evaluation of ventricular function and measurement of ventricular volumes by cardiovascular magnetic resonance imaging (MRI) is traditionally achieved using 2D cine steady-state free precession (SSFP) sequences [1]. In conventional procedure, two to four long-axis and ten to fifteen short-axis ventricular slices are prescribed to cover both ventricles. To minimize respiratory motion artifact, one or two slices are acquired at a time while the patients are asked to hold their breath for about five to fifteen seconds. However, this 2D breath-hold method contains several known shortcomings. Due to the relatively large slice thickness of 2D images compared to their in-plane resolution, stacks of contiguous 2D images cannot be reformatted in other planes. Therefore, ventricles must be imaged in different orientations with careful prescribing of imaging planes by expert operators. Further, very young or too-ill patients might not be able to hold their breath [2]. Even patients capable of perfect breath-holding may have some difficulties accomplishing a consistent level of breath-holding, resulting in inaccurate measurements of ventricular volumes [3].

A 3D cine SSFP sequence with an isotropic resolution prescribed in a straight imaging plane solves the shortcomings of 2D cine SSFP acquisitions since it does not require breath-holding, does not need

* Corresponding author at: Department of Cardiology, Boston Children's Hospital, 300 Longwood Avenue, Boston, MA 02115, USA.
E-mail address: lukas.braunstorfer@tum.de (L. Braunstorfer).

https://doi.org/10.1016/j.mri.2022.09.003
Received 10 February 2022; Received in revised form 18 August 2022; Accepted 13 September 2022
Available online 16 September 2022

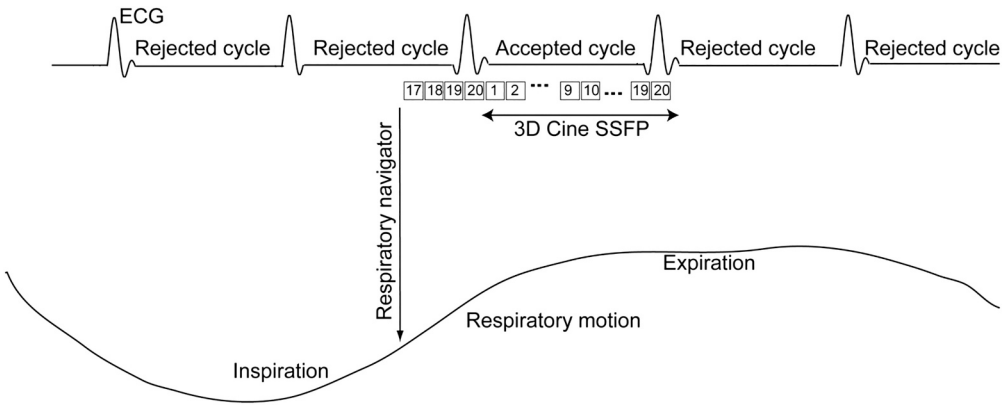

Fig. 1. Schematic diagram of the non-contrast free-breathing 3D cine sequence. A respiratory navigator is used to trigger the acquisition of 3D cine dataset during the transition from end-inspiration to expiration in two consecutive beats. The first beat is to allow the net magnetization vector to reach steady-state, and the second beat is used for data acquisition.

prescription of an angulated imaging plane, and—once acquired—can be reformatted into long-axis and short-axis views for ventricular volume measurements. In previous studies, 3D cine SSFP datasets have been acquired in a single breath-hold [4–12] using parallel imaging [13,14] and compressed sensing [15] techniques. However, single breath-hold 3D cine SSFP acquisition has not been widely adopted clinically because it sacrifices spatiotemporal resolution beyond that which is optimal for accurately measuring ventricular volumes [16]. Free-breathing acquisitions with respiratory motion compensation algorithms have been introduced to increase spatiotemporal resolution in 3D cine SSFP datasets [16–23], but they suffer from several shortcomings. These shortcomings include not sampling the entire cardiac cycle and requiring intravenous administration of gadolinium or iron-based contrast agents.

In this study, we developed and implemented a non-contrast free-breathing whole-heart 3D cine SSFP sequence with a novel 3D radial leaf trajectory that employs a conventional respiratory navigator to prospectively trigger the acquisition of high spatiotemporal resolution 3D cine data covering the entire cardiac cycle around respiratory end-expiration. The 3D radial dataset was then reconstructed offline using compressed sensing with total variation and wavelet transformation. The 3D cine images were compared with conventional 2D cine SSFP acquisitions in regards to image quality and ventricular volume measurements.

2. Methods

2.1. Non-contrast free-breathing whole-heart 3D Cine SSFP sequence

Fig. 1 illustrates the schematic diagram of the developed 3D cine SSFP sequence, which was prescribed to cover the whole-heart and great vessels in an axial orientation. A respiratory navigator (NAV) was placed at the dome of the right hemidiaphragm to continuously track respiratory motion. When a transition from inspiration to expiration was detected by the respiratory NAV, acquisition of the 3D cine dataset was started in the two consecutive beats. The 3D cine dataset acquired in the first beat was rejected since it did not cover the entire cardiac cycle due to the presence of respiratory NAV. In our implementation, at least three

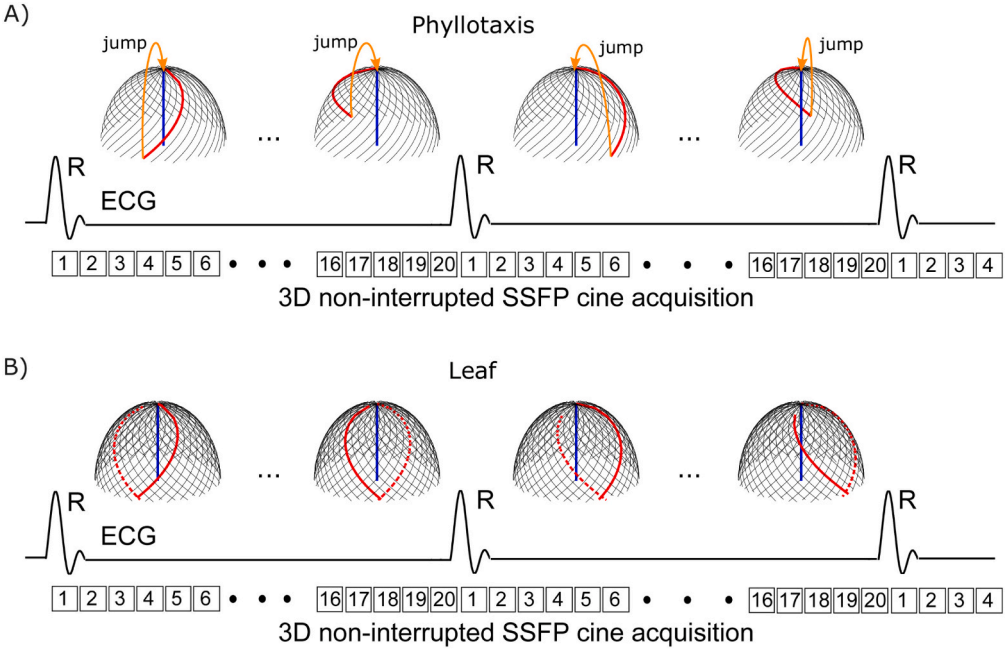

Fig. 2. 3D radial golden angle phyllotaxis (A) and leaf (B) trajectories for the non-contrast free-breathing 3D cine sequence binned into 20 cardiac phases. The phase jump during the large gradient change is indicated in the golden angle phyllotaxis trajectory.

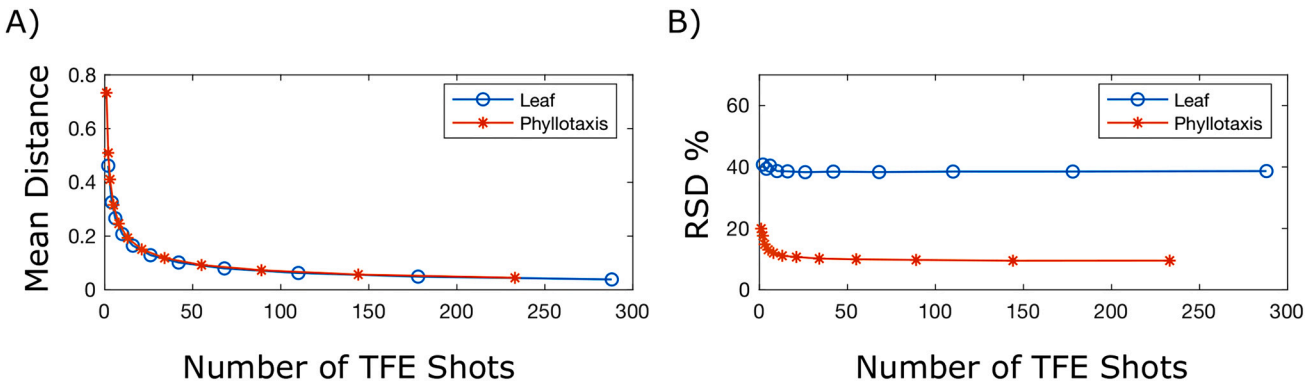

Fig. 3. A) Normalized mean difference and B) relative standard deviation (RSD) of the distance of each sampling point to its 4 closest neighbors for different number of Turbo Field Echo (TFE) shots in phyllotaxis and leaf trajectories.

cardiac phases from the first beat were needed to allow the net magnetization vector to reach steady-state [17]. After the transition from respiratory inspiration to expiration, if there were at least three cardiac phases in the first beat, we allowed the acquisition of 3D cine data in the second beat (i.e., following beat) and the 3D cine data acquired in the second beat was accepted for image reconstruction. Otherwise, we rejected the second beat. After completion of the second beat, the 3D cine acquisition paused, and the respiratory NAV monitored the respiratory motion to detect the next transition from inspiration to expiration. This procedure was repeated until all the prescribed k-space data was acquired.

Switching off the 3D cine acquisition during inspiration reduces the overall specific absorption rate and allows for T_1 recovery of the blood and myocardium. The penalty for switching off the 3D cine acquisition is that the steady-state is disrupted, and signal-to-noise-ratio and contrast-to-noise ratio modulation is introduced because of the T_1 relaxation [17]. To address these drawbacks and to minimize signal oscillations during the early transient phase, at least three cardiac phases were utilized to allow the net magnetization vector of the blood and myocardium to reach steady-state. These cardiac phases were not used for reconstruction as only the cardiac phases completely acquired within the entire next cardiac cycle were accepted for image reconstruction.

2.2. 3D radial leaf trajectory

A 3D cine MRI sequence requires a sizable amount of data and, as such, needs to be highly undersampled to reduce the imaging time to a clinically acceptable range. The 3D radial trajectories, such as kooshball [24,25] and golden angle phyllotaxis [26], are preferred over Cartesian in a highly accelerated imaging sequence because their undersampling artifact is less coherent [27]. The 3D golden angle phyllotaxis trajectory is advantageous over other radial trajectories since it has a highly uniform sampling distribution, i.e., low mean distances between sampling points [26]. The 3D golden angle phyllotaxis trajectory has, however, a disadvantage when applied to cine imaging. It has relatively large jumps from polar to azimuth plane after each interleaf, as shown in Fig. 2A. These jumps require a sudden gradient change that creates eddy current artifacts.

We developed a novel 3D radial leaf trajectory to reduce eddy current artifacts. In our leaf trajectory, we defined M interleaves (element of Fibonacci sequence), P shots per interleaf, and a temporal resolution of 20 phases. The spherical angles $\varphi_{1,n}$, $\varphi_{2,n}$, and θ_n were then defined as:

$$\varphi_{1,n} = \frac{2\pi}{360} \bullet n \bullet \varphi_{golden\ angle}, \tag{1}$$

$$\varphi_{2,n} = -\frac{2\pi}{360} \bullet n \bullet \varphi_{golden\ angle}, \tag{2}$$

$$\theta_n = \frac{\pi}{2}\sqrt{\frac{n}{N}}, \text{with } \varphi_{golden\ angle} = 137.5^\circ \text{and } n = 1 \text{ to } M \times P \tag{3}$$

$\varphi_{1,n}$, $\varphi_{2,n}$ describe two phyllotaxis distributions, both with opposing spiral directions. All spirals were sorted such that each downward spiral from the first distribution found an opposing upward spiral from the second distribution. This pair of downward and upward spirals created a leaf-shaped trajectory (Fig. 2B). Compared to 3D radial golden angle phyllotaxis trajectory, leaf pairs permit smoother k-space transitions from polar to azimuth plane with traversing the superior-inferior direction every other cardiac phase. Leaf pairs should reduce eddy current artifacts while maintaining the same low mean distances between neighboring points (Fig. 3A) and a larger relative standard deviation of the distance between each sampling point and its 4 closest neighbors (Fig. 3B). Supporting Video S1 displays dynamic behavior of golden angle phyllotaxis and leaf trajectories in 3D cine acquisitions with an exemplary setting of M = 21 and $P = 14$. The leaf trajectory was successfully implemented on a clinical scanner and used for the acquisition of non-contrast free-breathing accelerated 3D cine images.

2.3. Nonlinear iterative image reconstruction

To construct the highly undersampled 3D cine dataset, we used a compressed sensing reconstruction algorithm. For the minimization cost function, we utilized a slight modification of cost functions employed by XD-GRASP [28] and Sparse MRI [15] as:

$$\boldsymbol{d} = \underset{\boldsymbol{d}}{\operatorname{argmin}} \|\boldsymbol{F} \bullet \boldsymbol{C} \bullet \boldsymbol{d} - \boldsymbol{m}\|_2^2 + \lambda_1 TV(\boldsymbol{d}) + \lambda_2 \|\boldsymbol{\Psi} \bullet \boldsymbol{d}\|_1,$$

where $\boldsymbol{d}$ is the desired reconstructed 4D image, $\boldsymbol{m}$ is the acquired k-space data, $\boldsymbol{F}$ is the nonuniform fast Fourier transform operator, and $\boldsymbol{C}$ is the coil sensitivity maps. The following steps were performed to compute coil sensitivity maps: 1. Each radial k-space data point was cropped to keep only the inner 25% of readout points and zero-pad the remaining data; 2. A symmetric Hanning window was then applied to the cropped radial spokes to ensure a smooth transition of the signal in each radial spoke; 3. We performed nonuniform fast Fourier transform on the k-space data to generate an image from each coil. A combined image was then generated by calculating the root sum squares of the images from all the coils. The coil sensitivity map was then calculated by dividing the image from each coil by the combined image. TV indicates the finite-differences operator, also known as total-variations, which was applied along the cardiac motion dimension. $\boldsymbol{\Psi}$ indicates 3D 'Daubechies' spatio wavelet transform, which was applied for each cardiac phase individually [15]. λ_1 and λ_2 describe the regularization parameters for TV and wavelet transformation, respectively. Regularization parameters were determined using a two-dimensional refining iterative

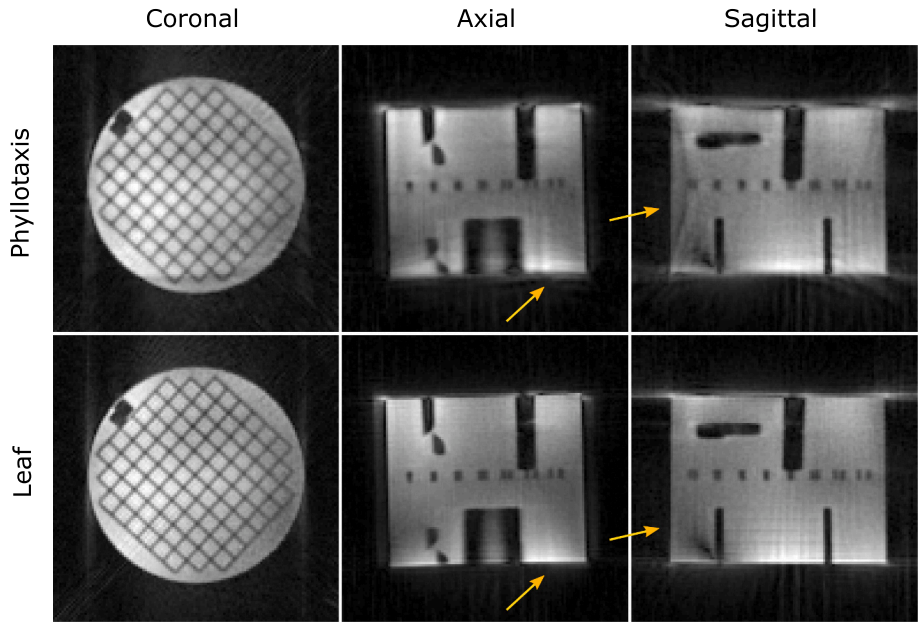

Fig. 4. Phantom study comparing phyllotaxis and leaf trajectories in an isotropic whole-heart 3D cine SSFP acquisition. Phantom images are shown in coronal, transversal, and sagittal views. Yellow arrows indicate less eddy current artifact and superior image quality for the leaf trajectory reconstruction compared to phyllotaxis. (For interpretation of the references to colour in this figure legend, the reader is referred to the web version of this article.)

grid search for minimizing streaking and blurring artifacts. A non-linear conjugate gradient method with backtracking line search was used for minimization [15]. Residual high frequency flickering was suppressed by adding a median filter along the cardiac motion dimension.

2.4. Phantom study

A phantom study was performed to evaluate the efficacy of the leaf trajectory and compare it with the phyllotaxis trajectory. A high-resolution static phantom was imaged using a 1.5 T Achieva-dStream Philips MRI scanner (Philips Medical Systems, Best, the Netherlands) and a 32-element receiver coil-array with the whole-heart 3D cine SSFP sequence. We repeated the whole-heart 3D cine SSFP acquisitions in an axial plane twice: first with phyllotaxis trajectory and second with leaf trajectory. The whole-heart 3D cine SSFP sequence had the following imaging parameters: field-of-view (FOV) = 250x250x250mm, acquired resolution = 2.0 mm^3 (isotropic), flip-angle (FA) = 60.0°, repetition-time (TR) = 3.3 ms, echo-time (TE) = 1.62 ms, acquired heart phases = 20, reconstructed heart phases = 30, bandwidth (BW) = 1.8 kHz, number of interleaves (M) = 144, number of shots per interleave (P) = 15, and undersampling rate = 11.4. The scan time of the whole-heart 3D cine SSFP acquisition was the same for both phyllotaxis and leaf trajectories.

2.5. Subjects

We performed a prospective study to assess the performance of our non-contrast free-breathing whole-heart 3D cine SSFP sequence with 3D radial leaf trajectory compared to the breath-hold 2D cine SSFP acquisition in clinical practice. Thirteen patients (7 male, median age 18 [range 11–26] years, median heart rate 79 [range 54–105] bpm) were included in the study. All included participants underwent a cardiovascular MRI examination that did not include administration of a contrast agent nor sedation. A written consent was acquired from all participants and the study was approved by our institutional review board committee.

2.6. Imaging protocols

A 1.5 T Achieva-dStream Philips MRI scanner was used for cardiovascular MRI examinations. A breath-hold 2D cine SSFP sequence with retrospective electrocardiogram gating was used to image all participants, resulting in the acquisition of a stack of ten to fifteen slices in the ventricular short-axis view. Two slices were acquired per breath-hold requiring the participants to hold their breath at end-expiration for about ten to fifteen seconds. The imaging parameters for the 2D cine SSFP acquisition were as follows: FOV = 260 × 260 mm, k-space trajectory Cartesian, spatial resolution = 1.80 × 1.80 mm, reconstructed spatial resolution = 1.25 × 1.25 mm, slice-thickness = 8.0 mm, slice-gap = 0.0–2.0 mm, FA = 60.0°, TR = 2.8 ms, TE = 1.4 ms, BW = 1.10 kHz, acquired heart-phases = 20, reconstructed heart-phases = 30, and compressed-SENSE ×2. At the end of the clinical exam, our non-contrast free-breathing whole-heart 3D cine SSFP sequence with 3D radial leaf trajectory was acquired in an axial plane with the following imaging parameters: FOV = 180-200 mm^3, spatial resolution = 2.0 mm^3 (isotropic), FA = 60.0°, TR = 2.9–3.1 ms, TE = 1.44–1.55 ms, BW = 1.74 kHz, acquired heart-phases = 20, reconstructed heart-phases = 30, number of interleaves (M) = 377, and number of shots per interleave (P) = 12.46 ± 2.47. Due to the different heart rates of the patients, P varied such that the acquisition of 20 cardiac phases within a cardiac cycle was guaranteed. Because the FOV was different for each patient, the undersampling rate varied. The average undersampling rate was 6.7 ± 1.25.

2.7. Image analysis

The breath-held 2D images were reconstructed on the scanner. The free-breathing 3D cine images were reconstructed offline using a high-performance computing cluster with 72.73 ± 15.37 GB RAM and 4 CPU units supported by the research computing group at our institution. The images were then transferred to a workstation and evaluated using MASS research software (Leiden University Medical Center). One physician experienced in cardiovascular MRI (JR) reformatted the 3D cine images into short-axis views similar to the 2D cine images and measured left and right ventricular end-diastolic volume (EDV) and end-

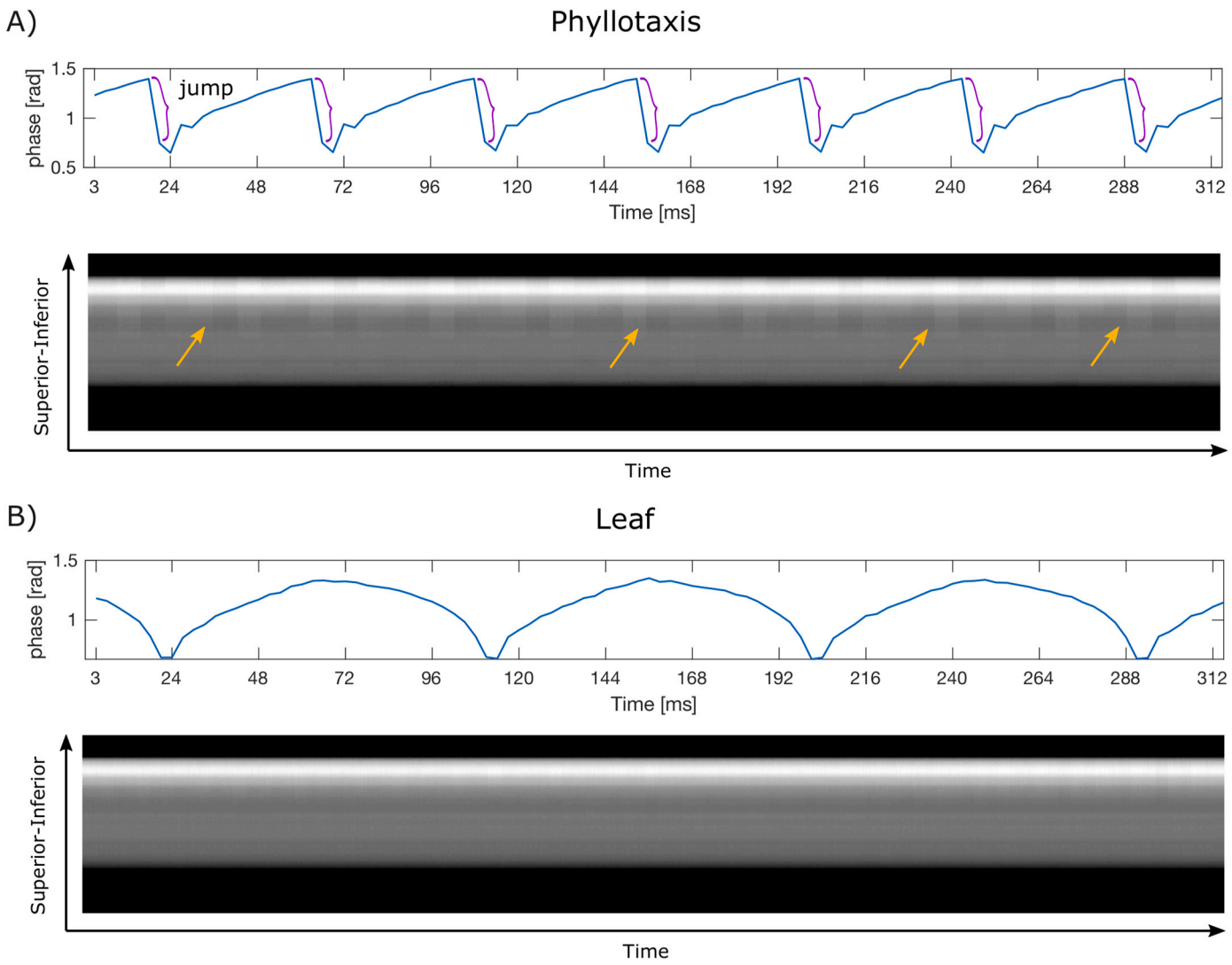

Fig. 5. Phase of center point of k-space in a 3D cine SSFP sequence with phyllotaxis (A) and leaf (B) trajectories. The phase jump during the large gradient change is visible (yellow arrows) in the center line of k-space along the superior-inferior direction in the golden angle phyllotaxis trajectory. (For interpretation of the references to colour in this figure legend, the reader is referred to the web version of this article.)

systolic volume (ESV) using a standard summation of disks approach. The image quality of the ventricular borders on the short-axis images was qualitatively scored by two clinicians (JR and LPB) based on a 4-point scale: 1) poor, 2) fair, 3) good, and 4) excellent [29].

2.8. Statistical analysis

Median and range or mean and standard deviation were used to report the statistics, as appropriate. Normality was tested using a Shapiro-Wilk test. Either a two-tailed paired *t*-test or a Wilcoxon signed-rank test was used to compare two groups of paired data with Gaussian and non-Gaussian distributions, respectively. The two tailed t-test was used to compare the volumetric measurements and the Wilcoxon signed-rank test was used to compare the image quality scores. A P-value ≤ 0.05 was considered statistically significant. The differences between 2D and 3D ventricular volumes were calculated, and Bland-Altman analysis and Pearson's correlation coefficient were used to compare the 2D and 3D ventricular volumes [29].

3. Results

3.1. Phantom study

The results of the phantom study are shown in Figs. 4 and 5. As shown in Fig. 4, the images from leaf trajectory have less artifact compared to phyllotaxis trajectory. Yellow arrows in Fig. 4 indicate artifacts which appear in the phyllotaxis reconstruction but are suppressed using the leaf trajectory. The projections in the superior-inferior direction of both phyllotaxis and leaf trajectories are compared in Fig. 5. The k-space jumps (indicated by yellow arrows) which occur in the phyllotaxis trajectory but are suppressed in the leaf trajectory are visible over the entire scan time

3.2. Subjects

All participants completed the imaging protocols successfully. The principal diagnoses of participants were as follows: left-sided obstructive lesions ($n = 4$, 2 with isolated aortic valve disease, 1 with coarctation of the aorta and bicuspid aortic valve, 1 with hypoplastic left heart syndrome palliated to a Fontan circulation), conotruncal abnormalities (n = 4; 3 tetralogy of Fallot and 1 double-outlet right ventricle

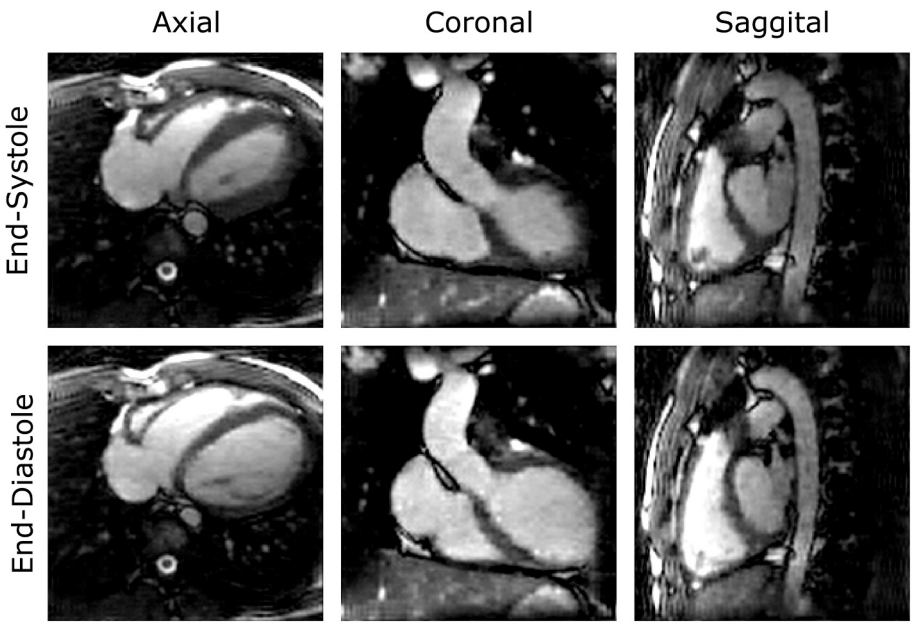

Fig. 6. Non-contrast free-breathing 3D cine images at end-diastolic and end-systolic cardiac phases from an 18 year old male patient with repaired tetralogy of Fallot.

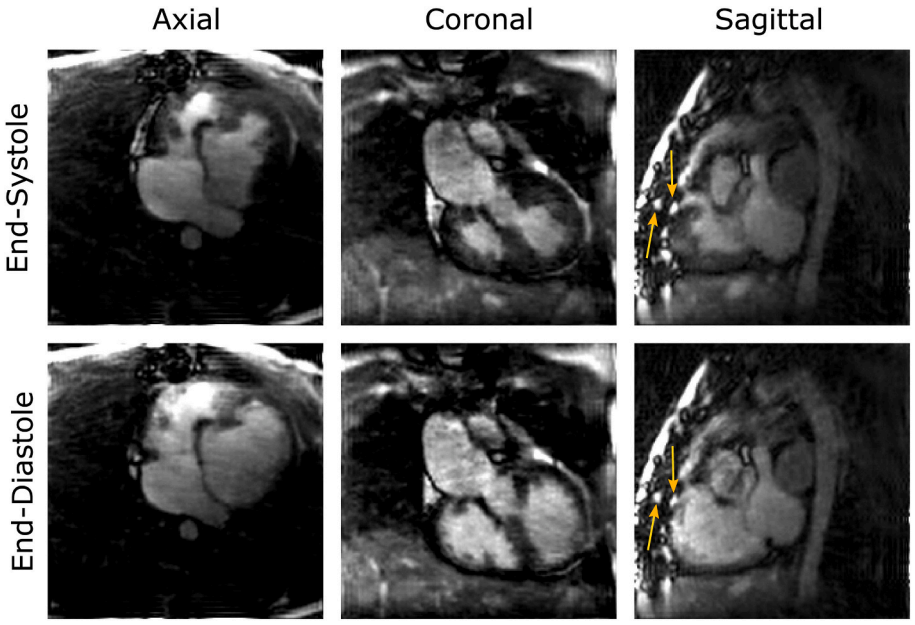

Fig. 7. Non-contrast free-breathing 3D cine images at end-diastolic and end-systolic cardiac phases from a 24 year old female patient with transposition of the great arteries after [arterial/atrial] switch operation. Arrows show the location of sternal wires. The image quality is negatively influenced by their presence.

with subpulmonic ventricular septal defect and pulmonary stenosis), simple left-to-right shunts ($n = 2$, 1 atrial septal defect, 1 ventricular septal defect), Marfan's syndrome ($n = 1$), cardiomyopathy (n = 1), and Ebstein anomaly of the tricuspid valve following Cone operation (n = 1).

3.3. Scan time and image quality

Figs. 6, 7, and Supporting Video S2 display examples of non-contrast free-breathing 3D cine images acquired from 3 patients. Fig. 8 compares the reformatted non-contrast free-breathing 3D cine images in the short-axis view with their corresponding breath-hold 2D cine images in 2 patients. Table 1 demonstrates the image quality score of 2D and 3D cine images by 2 clinicians. On average, the non-contrast free-breathing 3D cine images had lower image quality scores than the 2D images for both LV (3.44 ± 0.58 vs. 2.15 ± 0.6; p-value<0.01) and RV (3.19 ± 0.53 vs. 2.15 ± 0.48; p-value<0.01). Mean scan time and reconstruction time for the non-contrast free-breathing 3D cine sequence were 07:09 ± 01:31 min and 06:10 ± 1:28 h, respectively.

3.4. Ventricular volume measurements

Table 2 and Fig. 9 compare the left and right ventricular volumes calculated from 2D and 3D cine images. Of note, means of observed 3D cine measurements of EDVs were smaller (p-value$\leq$0.044 and systematic bias between 6 and 8%), while means of observed ESVs were comparable (p-value $\geq$0.190 and systematic bias $<$6%). There was excellent correlation between the ventricular volumes measured by non-contrast free-breathing 3D cine images and conventional breath-held 2D

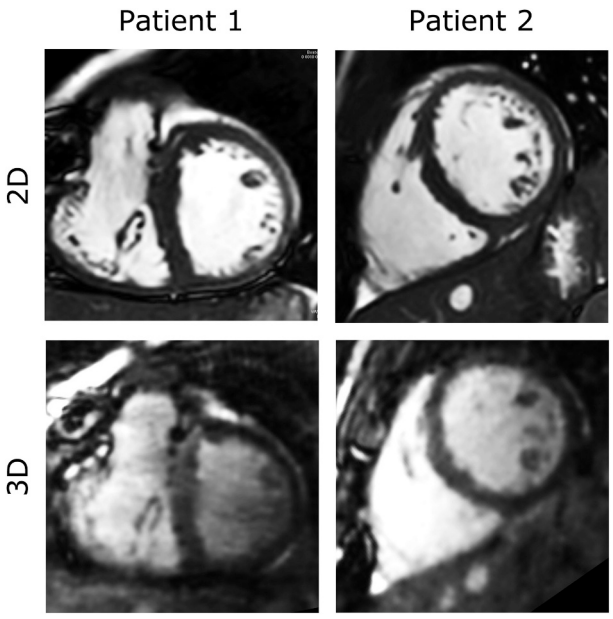

Fig. 8. 2D and 3D short-axis mid-ventricular cine images in diastolic cardiac phase acquired from a 24 year old female patient with transposition of the great arteries (Patient 1) and a 19 year old male patient with cardiomyopathy (Patient 2).

Table 1
Qualitative image quality score for 2D and 3D cine images ($n = 13$).

	Scorer 1		Scorer 2	
	LV	RV	LV	RV
2D images	3.08 ± 0.76	2.92 ± 0.64	3.81 ± 0.33	3.46 ± 0.38
3D images	1.54 ± 0.66	1.85 ± 0.38	2.77 ± 0.53	2.46 ± 0.56
P-value	<0.005	<0.005	<0.005	<0.005

Values are mean ± standard deviation. *P*-values are reported for Wilcoxon rank-sum tests. LV, left ventricle; and RV, right ventricle. Quality score values range from 1 (low quality) to 4 (high quality).

cine images (Pearson's correlation coefficient > 0.91).

4. Discussion

We developed and evaluated a non-contrast free-breathing whole-heart 3D cine SSFP sequence with a novel 3D radial leaf trajectory.

Table 2
Ventricular volumetric measurements for 2D and 3D cine images (n = 13).

	LV		RV	
	EDV	ESV	EDV	ESV
2D images (ml)	173.16 ± 47.42	78.46 ± 25.35	193.13 ± 49.38	102.42 ± 32.53
3D images (ml)	159.99 ± 42.99	79.12 ± 26.78	180.35 ± 46.08	97.18 ± 32.35
(2D—3D) (ml)	13.17 ± 19.63	−0.66 ± 13.26	12.77 ± 20.43	5.24 ± 13.62
(2D—3D) (%)	7.49 ± 10.64	−1.22 ± 17.14	6.54 ± 11.15	5.18 ± 14.73
P-value	**0.032**	0.860	**0.044**	0.190
Pearson's Correlation	0.910	0.910	0.911	0.912

Values are mean ± standard deviation. EDV, end-diastolic volume; ESV, end-systolic volume, LV, left ventricle; and RV, right ventricle. P-values are reported for paired *t*-tests.

This sequence uses standard diaphragmatic respiratory NAV technology to trigger 3D cine acquisition at end-expiration, maintains the equilibrium state of the net magnetization vector, acquires data throughout the entire cardiac cycle, and does not require administration of a contrast agent. Rather than using the k-space lines along the superior-inferior direction for respiratory motion compensation and continuously acquiring the 3D cine data over the entire respiratory cycle as a 5D dataset [23], we used respiratory NAV to trigger data acquisition at end-expiration to limit the specific absorption rate and improve the image quality [17]. We also employed a novel 3D radial leaf trajectory for 3D cine acquisition instead of 3D radial golden angle phyllotaxis trajectory because it has a smooth transition from polar to azimuth plane leading to less eddy current artifacts. This trajectory has the same low mean distances between neighboring sampling points as the phyllotaxis trajectory. The leaf trajectory has a larger relative standard deviation of sampling points compared to the phyllotaxis trajectory which could be beneficial in compressed sensing reconstruction algorithms since it increases randomness of the sampling points. Similar to our technique, Usman et al. [21] utilize a golden angle Cartesian trajectory with spiral profile ordering for a 3D cine acquisition of the whole-heart and vasculature. In such techniques, computational complexity is lower as gridding and re-gridding steps are not required. However, the novel leaf trajectory benefits from less coherent undersampling artifact as more randomness helps to recover missing k-space data in the compressed sensing reconstruction algorithms. Also, in a pure radial leaf trajectory, shorter TR values can be achieved. In addition, 3D radial leaf trajectory does not require fold-over suppression or a large FOV in fold-over direction to avoid wrap around artifact.

In a phantom study, we showed that leaf trajectory has a smooth transition from polar to azimuth plane leading to less artifact associated with jumps in gradients and eddy current. When applied to our prospective cohort, all the respiratory triggered non-contrast free-breathing whole-heart 3D cine SSFP acquisitions were successful, and the mean scan time was 07:09 ± 01:31 min. Observed ventricular EDVs from the 3D cine images were marginally smaller than the ones measured from the 2D cine acquisition, while observed ventricular ESVs were comparable. Biases in ventricular volumetric measurements were all <8%, which is consistent with observed inter-scan variability in congenital heart disease patients [30]. The 3D and 2D cine images had identical temporal resolution; however, reformatting the 3D images into a short-axis view decreased the spatial resolution of the 3D cine images compared to the 2D datasets. This difference could have been associated with lower ventricular volumes as we found [31,32]. Further, it is probable that physiologic changes in ventricular filling during breath-holding versus free-breathing contributed to the bias between ventricular volumes measured from 2D and 3D cine images. One other possible reason for underestimation of ventricular EDVs might be related to the image quality of the 3D cine dataset, as the contouring physician had difficulty discerning some free wall borders. Holst et al. [33] employed a 3D double golden angle whole-heart cine sequence to evaluate the amount of variation in LV EDV throughout the respiratory cycle in healthy adults. They showed that LV EDV was greatest during mid respiratory expiration and lowest during mid respiratory inspiration with a maximum difference of about 5% over a 25-min 3D cine whole-heart acquisition. The mean maximum LV EDV for their cohort of healthy adults was 159 ± 5 ml. For our cohort, the mean LV EDV was 159.99 ± 42.99 ml. Our patient population was composed of children and adults with and without significant congenital heart disease, many with very complex anatomy [34]. As a result, we observed a higher variance in our ventricular volume measurements across the cohort.

On average, the image quality score of our 3D cine images was nearly one grade lower than for the 2D datasets. The lower blood-to-myocardium contrast ratio and signal-to-noise ratio in the 3D cine images likely contributed to this finding. Blood and myocardium signal intensity was influenced by various factors in this study. In 2D acquisitions, unexcited blood flowing into the imaging plane creates bright

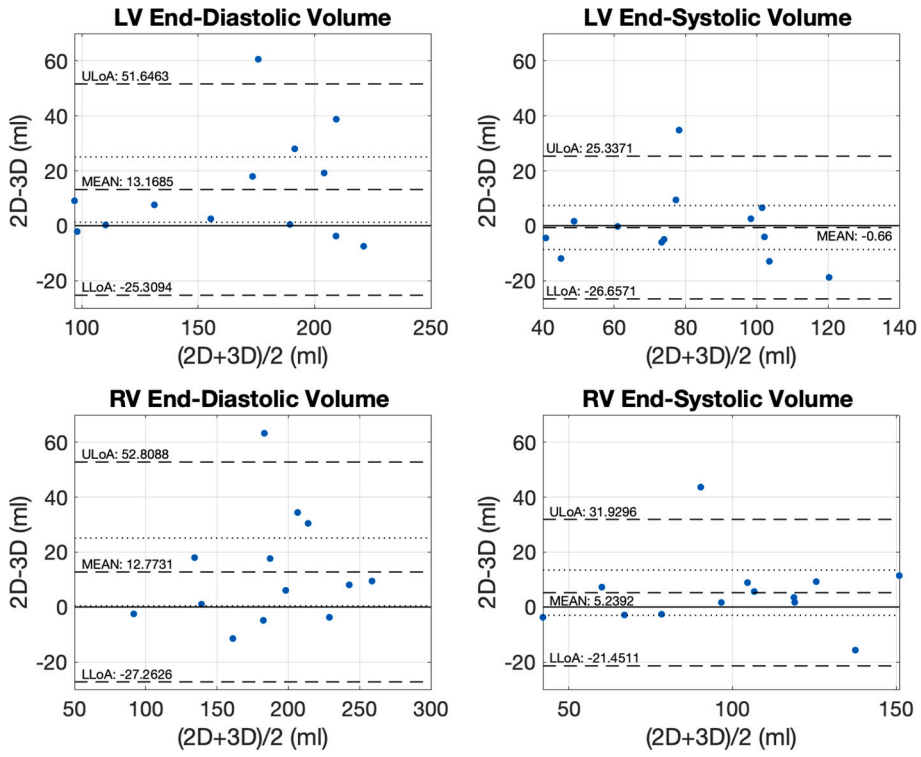

Fig. 9. Bland-Altman plots comparing left and right ventricular volumes computed from 2D and 3D cine images. The mean difference (bias) and 95% upper and lower limits of agreement (LOA) as well as the 95% confidence interval for the bias are shown in the figs. LV, left ventricle; and RV, right ventricle.

signal in ventricular cavities [35]. However, in the 3D acquisitions, the FOV and volume of excitation are larger, and the blood flowing into the imaging volume is already excited and saturated. The saturated inflowing blood creates darker signal in the ventricular cavities and reduces the image quality of the 3D cine images [35]. To reduce the saturation effect and improve the image quality, similar to Henningsson et al. [17], we acquired the 3D cine data only during end-expiration to allow the net magnetization vector of blood and myocardium to recover during inspiration. Other investigators [18,20,22] used administration of either gadolinium-based or iron-based T_1-shortening intravenous contrast agents to significantly improve the signal-to-noise and blood-to-myocardium contrast-to-noise ratio. These contrast agents are, however, associated with side effects including deposition in the brain [36] and anaphylaxis [37]. To avoid the use of contrast agents, Feng et al. [23] frequently interrupted the 3D cine acquisitions to nullify the signal from fat and improve the blood-to-myocardium contrast ratio and signal-to-noise ratio.

Based on the results of this study, we are optimistic about the clinical usefulness of our 3D cine sequence with a novel 3D radial leaf trajectory. It does not require breath-holding, eliminates the need for contrast agents, has an acceptable scan time, is easy to prescribe an imaging volume, and provides the reformatting advantages of a volumetric dataset. In the current implementation, the image quality of the 3D cine images is still lower than the conventional 2D cine datasets. Suppressing the signal from fat may help to further improve image quality [38]. The acquired k-space lines along the superior-inferior direction in the leaf trajectory could also be used to correct for residual respiratory motion left in the 3D cine datasets. Further, in our study, a basic implementation of coil sensitivity maps was used. Scanner-embedded coil sensitivity maps are expected to deliver higher quality and would presumably lead to an increase in the image quality.

Limitations of our study include the relatively small sample size. Additional differences between the 3D and 2D cine acquisitions might be revealed when analyzing a larger sample size. We did not include patients under anesthesia in this study because the addition of our experimental protocol would have prolonged their sedation time. However, we would expect increased image quality using the 3D cine sequence in patients under anesthesia since anesthetized patients commonly have a more regular breathing pattern and heart rate. A systematic optimization of the 3D cine parameters with the leaf trajectory remains to be performed. A 2.0 mm^3 spatial resolution and mean undersampling rate of 6.7 were chosen because they provided acceptable image quality and an average increase in scan time of 7.09 min. However, 7.09 min of scan time is still long for a spatial resolution of 2.0 mm^3. Irregularities in breathing patterns and cardiac cycle length could lead to an increased amount of rejected 3D cine data (i.e., decreased scan efficiency) and result in longer imaging time. Furthermore, we did not use a contrast agent in our free-breathing 3D cine acquisitions to improve signal-to-noise ratio or spatial resolution. A 2.0 mm^3 spatial resolution was chosen to maintain reasonable signal-to-noise ratio and image quality. Although administration of contrast agent would be helpful to improve signal-to-noise ratio and spatial resolution [39], our aim was to develop a needle-free 3D cine acquisition that does not require a contrast agent; thus, increasing the safety and patient comfort associated with CMR examinations. The respiratory navigator employed in our free-breathing 3D cine acquisitions has some limitations. It does not directly measure the respiratory motion of the heart and uses the respiratory motion of the right hemidiaphragm as a surrogate. It also requires planning that may require extra time from imaging experts to prescribe the position of the respiratory navigator. Finally, respiratory drift may occur during the free-breathing acquisitions. Even accounting for these limitations, the respiratory navigator is one of the most frequently used techniques in clinical practice. The reconstruction time of the 3D cine images is prohibitively long for real-time assessment of cardiac function while the patient is in the scanner. However, we expect to significantly reduce the reconstruction time of 3D cine images in the future by using an artificial-intelligence-based reconstruction algorithm [40–43].

5. Conclusion

We developed a non-contrast free-breathing whole-heart 3D cine SSFP sequence with a novel radial leaf trajectory. Observed ventricular end-diastolic volume measurements using this sequence were slightly smaller than those obtained with a conventional breath-hold 2D cine SSFP acquisition. Scan time was within a clinically acceptable range. Such 3D cine acquisitions eliminate the need for breath-holding, contrast agents, and plane-planning at the time of acquisition; and thus, they simplify scanning.

Funding sources

This work is supported by NIH-NHLBI (1R01HL149807-01) and German Academic Exchange Service / Biomedical Exchange Program (DAAD / BMEP).

Author statement

Conceptualization: LB, MHM. Data curation: LB, RJG, MHM. Formal analysis: LB, JP, MHM. Funding acquisition: MHM. Investigation: LB, MHM. Methodology: LB, MHM. Project administration: MHM. Resources: MHM. Software: LB, JP, RJG, MHM. Supervision: MHM. Validation: LB, JP, JR, LPB, MHM. Visualization: LB, JR, LPB, MHM. Writing - original draft: LB, JR, MHM. Writing - review & editing: all.

Supplementary data to this article can be found online at https://doi.org/10.1016/j.mri.2022.09.003.

References

[1] Kramer CM, Barkhausen J, Flamm SD, Kim RJ, Nagel E. Standardized cardiovascular magnetic resonance (CMR) protocols 2013 update. J Cardiovasc Magn Reson 2013;15(1):91.
[2] Jahnke C, Paetsch I, Achenbach S, Schnackenburg B, Gebker R, Fleck E, et al. Coronary MR imaging: breath-hold capability and patterns, coronary artery rest periods, and beta-blocker use. Radiology 2006;239(1):71–8.
[3] Swingen C, Seethamraju RT, Jerosch-Herold M. An approach to the three-dimensional display of left ventricular function and viability using MRI. Int J Card Imaging 2003;19(4):325–36.
[4] Jung BA, Hennig J, Scheffler K. Single-breathhold 3D-trueFISP cine cardiac imaging. Magn Reson Med 2002;48(5):921–5.
[5] Makowski MR, Wiethoff AJ, Jansen CH, Uribe S, Parish V, Schuster A, et al. Single breath-hold assessment of cardiac function using an accelerated 3D single breath-hold acquisition technique–comparison of an intravascular and extravascular contrast agent. J Cardiovasc Magn Reson 2012;14(1):53.
[6] Parish V, Hussain T, Beerbaum P, Greil G, Nagel E, Razavi R, et al. Single breath-hold assessment of ventricular volumes using 32-channel coil technology and an extracellular contrast agent. J Magn Reson Imaging 2010;31(4):838–44.
[7] Maredia N, Kozerke S, Larghat A, Abidin N, Greenwood JP, Boesiger P, et al. Measurement of left ventricular dimensions with contrast-enhanced three-dimensional cine imaging facilitated by k-t SENSE. J Cardiovasc Magn Reson 2008;10:27.
[8] Hamdan A, Kelle S, Schnackenburg B, Wellnhofer E, Fleck E, Nagel E. Single-breathhold four-dimensional assessment of left ventricular volumes and function using k-t BLAST after application of extracellular contrast agent at 3 Tesla. J Magn Reson Imaging 2008;27(5):1028–36.
[9] Kozerke S, Tsao J, Razavi R, Boesiger P. Accelerating cardiac cine 3D imaging using k-t BLAST. Magn Reson Med 2004;52(1):19–26.
[10] Peters DC, Ennis DB, Rohatgi P, Syed MA, McVeigh ER, Arai AE. 3D breath-held cardiac function with projection reconstruction in steady state free precession validated using 2D cine MRI. J Magn Reson Imaging 2004;20(3):411–6.
[11] Barkauskas KJ, Rajiah P, Ashwath R, Hamilton JI, Chen Y, Ma D, et al. Quantification of left ventricular functional parameter values using 3D spiral bSSFP and through-time non-Cartesian GRAPPA. J Cardiovasc Magn Reson 2014;16:65.
[12] Wetzl J, Schmidt M, Pontana F, Longere B, Lugauer F, Maier A, et al. Single-breath-hold 3-D CINE imaging of the left ventricle using Cartesian sampling. MAGMA 2017. https://doi.org/10.1007/s10334-017-0624-1.
[13] Pruessmann KP, Weiger M, Scheidegger MB, Boesiger P. SENSE: sensitivity encoding for fast MRI. Magn Reson Med 1999;42(5):952–62.
[14] Griswold MA, Jakob PM, Heidemann RM, Nittka M, Jellus V, Wang J, et al. Generalized autocalibrating partially parallel acquisitions (GRAPPA). Magn Reson Med 2002;47(6):1202–10.
[15] Lustig M, Donoho D, Pauly JM. Sparse MRI: the application of compressed sensing for rapid MR imaging. Magn Reson Med 2007;58(6):1182–95.
[16] Uribe S, Muthurangu V, Boubertakh R, Schaeffter T, Razavi R, Hill DL, et al. Whole-heart cine MRI using real-time respiratory self-gating. Magn Reson Med 2007;57(3):606–13.
[17] Henningsson M, Chan RH, Goddu B, Goepfert LA, Razavi R, Botnar RM, et al. Contrast-enhanced specific absorption rate-efficient 3D cardiac cine with respiratory-triggered radiofrequency gating. J Magn Reson Imaging 2013;37(4):986–92.
[18] Pang J, Sharif B, Fan Z, Bi X, Arsanjani R, Berman DS, et al. ECG and navigator-free four-dimensional whole-heart coronary MRA for simultaneous visualization of cardiac anatomy and function. Magn Reson Med 2014;72(5):1208–17.
[19] Coppo S, Piccini D, Bonanno G, Chaptinel J, Vincenti G, Feliciano H, et al. Free-running 4D whole-heart self-navigated golden angle MRI: Initial results. Magn Reson Med 2015;74(5):1306–16.
[20] Han F, Zhou Z, Han E, Gao Y, Nguyen KL, Finn JP, et al. Self-gated 4D multiphase, steady-state imaging with contrast enhancement (MUSIC) using rotating cartesian K-space (ROCK): Validation in children with congenital heart disease. Magn Reson Med 2017;78(2):472–83.
[21] Usman M, Ruijsink B, Nazir MS, Cruz G, Prieto C. Free breathing whole-heart 3D CINE MRI with self-gated Cartesian trajectory. Magn Reson Imaging 2017;38:129–37.
[22] Moghari MH, Barthur A, Amaral ME, Geva T, Powell AJ. Free-breathing whole-heart 3D cine magnetic resonance imaging with prospective respiratory motion compensation. Magn Reson Med 2018;80(1):181–9.
[23] Feng L, Coppo S, Piccini D, Yerly J, Lim RP, Masci PG, et al. 5D whole-heart sparse MRI. Magn Reson Med 2018;79(2):826–38.
[24] Stehning C, Bornert P, Nehrke K, Eggers H, Stuber M. Free-breathing whole-heart coronary MRA with 3D radial SSFP and self-navigated image reconstruction. Magn Reson Med 2005;54(2):476–80.
[25] Nam S, Akcakaya M, Basha T, Stehning C, Manning WJ, Tarokh V, et al. Compressed sensing reconstruction for whole-heart imaging with 3D radial trajectories: a graphics processing unit implementation. Magn Reson Med 2013;69(1):91–102.
[26] Piccini D, Littmann A, Nielles-Vallespin S, Zenge MO. Spiral phyllotaxis: the natural way to construct a 3D radial trajectory in MRI. Magn Reson Med 2011;66(4):1049–56.
[27] Shu Y, Riederer SJ, Bernstein MA. Three-dimensional MRI with an undersampled spherical shells trajectory. Magn Reson Med 2006;56(3):553–62.
[28] Feng L, Axel L, Chandarana H, Block KT, Sodickson DK, Otazo R. XD-GRASP: Golden-angle radial MRI with reconstruction of extra motion-state dimensions using compressed sensing. Magn Reson Med 2016;75(2):775–88.
[29] Bland JM, Altman DG. Statistical methods for assessing agreement between two methods of clinical measurement. Lancet 1986;1(8476):307–10.
[30] Blalock SE, Banka P, Geva T, Powell AJ, Zhou J, Prakash A. Interstudy variability in cardiac magnetic resonance imaging measurements of ventricular volume, mass, and ejection fraction in repaired tetralogy of Fallot: a prospective observational study. J Magn Reson Imaging 2013;38(4):829–35.
[31] Miller S, Simonetti OP, Carr J, Kramer U, Finn JP. MR Imaging of the heart with cine true fast imaging with steady-state precession: influence of spatial and temporal resolutions on left ventricular functional parameters. Radiology 2002;223(1):263–9.
[32] Matthew S, Gandy SJ, Nicholas RS, Waugh SA, Crowe EA, Lerski RA, et al. Quantitative analysis of cardiac left ventricular variables obtained by MRI at 3 T: a pre- and post-contrast comparison. Br J Radiol 2012;85(1015):e343–7.
[33] Holst K, Ugander M, Sigfridsson A. Respiratory variation in left ventricular cardiac function with 3D double golden-angle whole-heart cine imaging. Magn Reson Med 2018;79(5):2693–701.
[34] Pace DF, Dalca AV, Brosch T, Geva T, Powell AJ, Weese J, et al. Learned iterative segmentation of highly variable anatomy from limited data: Applications to whole heart segmentation for congenital heart disease. Med Image Anal 2022;80:102469.
[35] Nezafat R, Herzka D, Stehning C, Peters DC, Nehrke K, Manning WJ. Inflow quantification in three-dimensional cardiovascular MR imaging. J Magn Reson Imaging 2008;28(5):1273–9.
[36] Ranga A, Agarwal Y, Garg KJ. Gadolinium based contrast agents in current practice: Risks of accumulation and toxicity in patients with normal renal function. The Indian J Radiol Imag 2017;27(2):141–7.
[37] DeLoughery TG. Risk of anaphylaxis with intravenous iron products. JAMA 2016;315(20):2232.
[38] Lu A, Brodsky E, Grist TM, Block WF. Rapid fat-suppressed isotropic steady-state free precession imaging using true 3D multiple-half-echo projection reconstruction. Magn Reson Med 2005;53(3):692–9.
[39] Roy CW, Di Sopra L, Whitehead KK, Piccini D, Yerly J, Heerfordt J, et al. Free-running cardiac and respiratory motion-resolved 5D whole-heart coronary cardiovascular magnetic resonance angiography in pediatric cardiac patients using ferumoxytol. J Cardiovasc Magn Reson 2022;24(1).
[40] Hyun CM, Kim HP, Lee SM, Lee S, Seo JK. Deep learning for undersampled MRI reconstruction. Phys Med Biol 2018;63(13):135007.
[41] Hammernik K, Klatzer T, Kobler E, Recht MP, Sodickson DK, Pock T, et al. Learning a variational network for reconstruction of accelerated MRI data. Magn Reson Med 2018;79(6):3055–71.
[42] Yang G, Yu S, Dong H, Slabaugh G, Dragotti PL, Ye X, et al. DAGAN: deep de-aliasing generative adversarial networks for fast compressed sensing MRI reconstruction. IEEE Trans Med Imaging 2018;37(6):1310–21.
[43] Kustner T, Fuin N, Hammernik K, Bustin A, Qi H, Hajhosseiny R, et al. CINENet: deep learning-based 3D cardiac CINE MRI reconstruction with multi-coil complex-valued 4D spatio-temporal convolutions. Sci Rep 2020;10(1):13710.